Chemical Engineering Journal 489 (2024) 150973

Contents lists available at ScienceDirect

Chemical Engineering Journal

journal homepage: www.elsevier.com/locate/cej

Advancing Li_3VO_4 as a high-performance anode material for use in lithium-ion batteries and lithium-ion capacitors

Yu-Sheng Hsiao [a], Jen-Hsien Huang [b], Lin-Yang Weng [a], Ta-Hung Cheng [a,c], Han-Hsin Chiang [d], Cheng-Zhang Lu [d], Huei-Chu Weng [e,*], Lars Thomsen [f], Bruce Cowie [f], Wei Kong Pang [g,*], Yu-Ching Huang [c,*]

[a] Department of Materials Science and Engineering, National Taiwan University of Science and Technology, No. 43, Sec. 4, Keelung Road, Da-an District, Taipei, 10607, Taiwan
[b] Department of Green Material Technology, Green Technology Research Institute, CPC Corporation, No.2, Zuonan Rd., Nanzi District, Kaohsiung City, 81126, Taiwan
[c] Department of Materials Engineering, Ming Chi University of Technology, 84 Gungjuan Road, Taishan District, New Taipei City, 24301, Taiwan
[d] Material and Chemical Research Laboratories, Industrial Technology Research Institute, No. 195, Chung Hsing Road, Chutung, Hsinchu 31040, Taiwan
[e] Department of Mechanical Engineering, Chung Yuan Christian University, No. 200, Chungpei Road, Chungli District, Taoyuan City 32023, Taiwan
[f] Australian Synchrotron, Australian Nuclear Science and Technology Organization, Clayton Victoria 3168, Australia
[g] Faculty of Engineering, Institute for Superconducting & Electronic Materials, University of Wollongong, Wollongong, NSW, Australia

ARTICLE INFO

Keywords:
Li_3VO_4
Doping
Anode
Lithium-ion battery
Lithium-ion capacitor

ABSTRACT

Li_3VO_4 (LVO) is a promising anode material for use in Li-ion batteries (LIBs) owing to its safe discharge plateau and high capacity. However, its moderate Li^+-diffusion coefficient and low electrical conductivity pose challenges to its widespread use in the LIB industry. In this study, hexavalent tungsten ions (W^{6+}) were introduced to boost electrochemical kinetics, and W^{6+}-doped LVO microspheres were successfully prepared using a spray-drying approach. Density functional theory (DFT) calculations reveal that the enhanced electronic conductivity and improved oxygen lattice following W^{6+} doping is possibly due to the development of a mid-gap state positioned above the valence band maximum. The doped LVO displayed excellent electrochemical performance, including a superior rate capability (288.9 mAh/g at 10C) and remarkable cycling stability (capacity fading of only 8.6 % over 200 cycles at 6C), which is ascribable to improved electrical conductivity and Li^+ insertion/extraction. In addition, we also fabricated a 3.7 V full LIB with a W^{6+}-doped LVO anode and a $LiNi_{0.5}Mn_{1.5}O_4$ (LNMO) cathode, and a lithium-ion capacitor (LIC) with an energy density of 131.8 Wh/kg using the modified LVO and active carbon (AC). This study demonstrates the potential of W^{6+}-doped LVO for use in energy-storage applications.

1. Introduction

Energy storage has recently become a prominent issue, primarily driven by the substantial increase in energy consumption and associated global environmental concerns. Lithium-ion batteries (LIBs) have gained significant attention for use in a wide range of applications, including portable devices and electric vehicles (EVs). This popularity stems from characteristics that include their lightweight designs, high energy densities, and long cycling lifespans. The primary demands of LIBs for practical use in large-scale energy-storage systems include high safety, power density, energy density, and cycling stability. However, traditional graphite anodes are unable to meet these requirements owing to their comparatively sluggish kinetics. Additionally, the development of lithium dendrites at a low operating potential of approximately 0.1 V (vs. Li/Li^+) presents safety concerns [1]. Hence, investigating novel anode materials with superior safety characteristics, desirable electrochemical properties, and tailored for a wide range of applications is imperative.

Spinel-type lithium titanate ($Li_4Ti_5O_{12}$, LTO), with its long flat charge/discharge plateau at 1.55 V (vs. Li^+/Li), prevents the formation of lithium dendrites and exhibits a high level of safety as a consequence [2]. In addition, zero-strain LTO demonstrates an exceptional rate capability and a long cycling life; hence, it is a potential alternative to graphite for use in various applications. Unfortunately, the limited

* Corresponding authors.
E-mail addresses: hcweng@cycu.edu.tw (H.-C. Weng), wkpang@uow.edu.au (W. Kong Pang), huangyc@mail.mcut.edu.tw (Y.-C. Huang).

https://doi.org/10.1016/j.cej.2024.150973
Received 7 January 2024; Received in revised form 7 March 2024; Accepted 2 April 2024
Available online 3 April 2024

theoretical capacity (175 mAh/g) of LTO results in a low energy density, which restricts its use in current applications [3]. $TiNb_2O_7$ (TNO) has been explored as an alternative anode material; it has an operating potential similar to that of LTO, while offering a significantly larger theoretical capacity (387 mAh/g) [4]. The redox potential of TNO of 1.5 V (vs. Li^+/Li), based on the Ti^{4+}/Ti^{3+} and Nb^{5+}/Nb^{4+} couples, prevents the formation of Li dendrites and ensures safety [5]. However, this high redox potential unavoidably results in a low full-cell voltage, which consequently affects the overall energy density of the system. Therefore, the use of TNO has led to insufficiently improved LIB energy densities.

Li_3VO_4 (LVO) is attracting increasing levels of interest as a novel anode material. LVO possesses an intercalation potential that falls between that of LTO and graphite, specifically in the 0.5–1.0 V range vs. Li^+/Li [6]. Furthermore, it delivers a high theoretical capacity of 397 mAh/g, which corresponds to double Li intercalation into the Li_3VO_4 structure and is competitive with that of graphite (372 mAh/g) [7]. The volume expansion associated with the reversible phase transformation between Li_3VO_4 and Li_5VO_4 is only 4 % during charging/discharging [8]; this characteristic contributes to the impressive cycling stability of LVO, which is among the most promising candidates for meeting the requirements of high safety, high energy density, and long lifespan owing to the advantages presented above. However, in a similar manner to other metal oxides, LVO also encounters the drawback of poor conductivity ($<10^{-10}$ S/m), resulting in a poor rate capability [9]. Several strategies have been proposed to improve the rate performance of LVO, including the creation of nanostructures to shorten the Li^+-diffusion pathway [10,11], surface modification using carbonaceous materials [12], preparing composites with graphene [13] or carbon nanotubes [14], and ionic doping [15,16]. Among these approaches, ionic doping is the only method that directly enhances electronic conductivity within the LVO crystal, resulting in reduced polarization.

In this study, we prepared W^{6+}-doped LVO using a spray-drying method. The electronic structure of LVO can be altered by substituting V^{5+} ions for W^{6+} to form a mid-gap state above the valence band maximum. As a result, the doped LVO exhibits a narrower bandgap and improved conductivity, leading to a superior rate capability. We show that the doped LVO delivers a capacity of 288.9 mAh/g at 10C which is 10.52-times larger than that of the pristine sample. Furthermore, a full LIB containing LVO and $LiNi_{0.5}Mn_{1.5}O_4$ (LNMO), and a hybrid lithium-ion capacitor (LIC) based on LVO and active carbon (AC), were fabricated to assess their practical potential.

2. Experimental section

2.1. Material synthesis

Pristine and doped LVOs were synthesized using a spray-drying method. Initially, a composition was prepared by dispersing V_2O_5 (247.9 g) and Li_2CO_3 (317.2 g) in deionized water (1300 mL). The precursor solution was then processed using a circulation-type wet grinder (JUSTNANO JBM-C020), followed by high-energy ball milling at ambient temperature and 2000 rpm, using ZrO_2 beads 50, 100, and 200 μm in diameter. The homogenized slurry was then pumped to a pilot-scale spray dryer (OHKAWARA KAKOHKI Co., LTD, model L-8i, No. 145874) with the spray-drying outlet temperature maintained at 130 °C. Spray-dried precursor powders were heated in air at 600 °C for 10 h to form orthorhombic LVO. W^{6+}-doped LVO was prepared using H_2WO_4 as the dopant. Similar procedures were used to prepare $Li_3V_{1-x}W_xO_4$ (x = 0.025, 0.05, 0.075, and 0.10) samples by adding specified quantities of H_2WO_4 to the precursor solution. $Li_3V_{1-x}W_xO_4$ samples doped at levels of 0.025, 0.05, 0.075, and 0.10 (x) are referred to as: 20.5-LVO, 5-LVO, 70.5-LVO, and 10-LVO, respectively.

2.2. Material characterizations and computational details

Material and electrochemical characterization, as well as computational details, are provided in the Supporting Information.

3. Results and discussion

Neutrons interact with atomic nuclei with scattering lengths that are independent of elemental atomic number, which sets them apart from X-rays. Integrating X-ray and neutron powder diffraction techniques facilitates comprehensive and precise crystallographic elucidation. In this study, we acquired both neutron powder diffraction (NPD) and X-ray diffraction (XRD) data for pristine and doped LVO samples, with respective patterns displayed in Fig. 1a and b, respectively. All samples show very similar intensity profiles that reveal that both pristine and doped LVO have orthorhombic structures (space group: *Pmn*21), consistent with the literature [17], with very similar positions of most reflections. The secondary-phase (vanadium carbide (VC) and Li_2CO_3, as shown in Fig. 1b) signals were observed to increase with increasing W-doping concentration.

The crystallographic structures and phase compositions of the pristine and doped LVO samples were obtained by further Rietveld-refining the NPD and XRD data, with refined and fitted profiles shown in Fig. 1c and d. Refined structural data for each sample are listed in Tables S1–S5, and suggest that W^{6+} ions are located at tetrahedral V sites (2a) in the crystal structure, with negligible lattice-parameter (a, b, and c) variations (Fig. 1e) despite V^{5+} ions (0.355 Å, CN = 4) substituted for larger W^{6+} ions (0.42 Å, coordination number (CN) = 4). It should be noted that the refined W-occupation percentages are slightly lower than the nominal W concentrations (Fig. 1f), with the weight fractions of the secondary phases (VC and Li_2CO_3) increasing with increasing W concentration. Based on the observed results, we conclude that Li and V are partially excluded from the structure to achieve charge neutrality when higher-valence W^{6+} is introduced into the orthorhombic phase. In other words, the doped structures are defective, with endothermic defect formation leading to solids with enhanced electrical conductivities owing to the migration of ions into holes [18].

The surface morphologies of the pristine and doped LVO were investigated by scanning electron microscopy (SEM). The spray-dried samples exhibited typical spherical morphologies (Fig. 2a–e). The pristine sample (Fig. 2a) has a smooth surface without any noticeable features. In contrast, the doped LVOs samples (Fig. 2b–e) exhibit rougher surfaces with prominent grain boundaries, with surface roughness increasing with W^{6+} concentration. Fig. 2e shows that the 10-LVO sample has grains that are 0.23–0.55 μm in size. The particle-size distributions of LVOs doped with various concentrations of W^{6+} are shown in Fig. S1. All samples exhibit multimodal distributions with very similar mean particle sizes (~1.84 μm). Additionally, these samples have almost identical true and tapped densities (Fig. 2f), with values of approximately 2.59 and 1.05 g/cm^3, respectively. The surface areas of the samples, as calculated from the N_2-adsorption–desorption isotherms, are shown in Fig. 2f. The pristine LVO sample has a surface area of 1.195 m^2/g, which was observed to increase with increasing W^{6+} concentration to a value of 4.486 m^2/g for 10-LVO, which is ascribable to increasing surface roughness. A rough surface endows the doped LVO with a high interfacial area, which is advantageous for ion transfer during lithiation/delithiation.

Internal structure and chemical composition were monitored using focused-ion-beam (FIB) SEM [19]. A Pt layer was applied to 5-LVO prior to the FIB-milling process to protect its surface from ion-beam radiation damage. The cross-sectional FIB-SEM image of 5-LVO (Fig. 2g) reveals a uniform porous structure with grains that are well-connected with large neckings, indicative of thermal-treatment success. The continuous internal pore structure not only offers additional space for accommodating volume expansion, but also creates more electrode/electrolyte interfaces for Li^+-ion transfer during lithiation/delithiation. Moreover, good necking between 5-LVO grains also facilitates charge transfer. The corresponding energy-dispersive X-ray spectroscopy (EDS) O, V, and W maps (Fig. 2h–k) reveal that all the elements are uniformly distributed

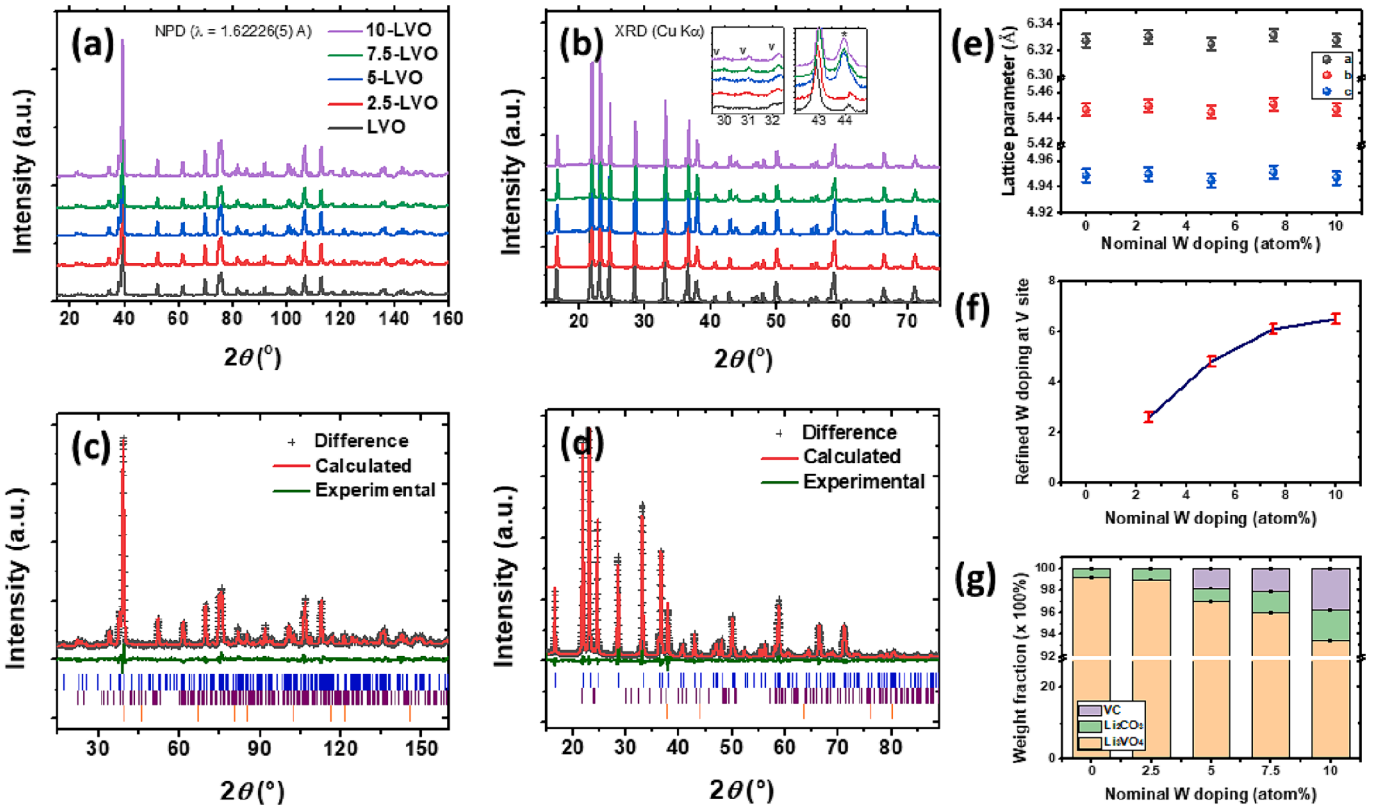

Fig. 1. Crystallographic investigation of the LVO samples. (a) NPD and (b) XRD data of LVO samples with the insets in (b) showing the reflections of VC (denoted as *) and Li_2CO_3 (denoted as V) impurities; refined fitness profiles of (c) NPD and (d) XRD of 5-LVO (reflection bars: blue (Li_2CO_3), purple (Li_3VO_4), and orange (VC)); (e) lattice parameters variation, (f) W occupancy variation at V site, and (g) the phase fractions upon W doping. (For interpretation of the references to colour in this figure legend, the reader is referred to the web version of this article.)

within the 10-LVO sample, indicating the W^{6+} ions are homogeneously doped in LVO.

Fourier-transform infrared (FTIR) and Raman spectroscopies were used to obtain structural information for the doped-LVO samples. Fig. 3a shows that LVO exhibits two strong FTIR peaks at 810 and 460 cm^{-1} that are attributable to asymmetric V − O and symmetric V − O − V stretching vibrations, respectively [20]. The other two peaks observed at 1430 and 1480 cm^{-1} are associated with CO_3^{2-} stretching vibrations [21] and are well aligned with the elevated Li_2CO_3 content, as evidenced by diffraction data acquired for doped LVOs with higher W contents. The Raman spectra (Fig. 3b) reveal characteristic peaks between 200 and 500 cm^{-1} and 750 and 950 cm^{-1} that are consistent with previous reports [10,13]. The Raman peaks at 817 and 789 cm^{-1} are ascribable to symmetric and asymmetric VO_4^{3-} stretching vibrations [20]. The observed trend unequivocally reveals that Raman intensity decreases with increasing W^{6+}-doping concentration, which suggests that incorporating W^{6+} induces a heightened disordered state [22], consistent with the enhanced crystallographic structure derived through combined NPD and XRD refinement.

Considering that the V − O bond significantly affects the electrochemical performance of LVO, synchrotron-based soft X-ray absorption spectroscopy (SXR) was employed to characterize the local V and O elemental environments in the LVO samples upon W doping. Fig. 3c displays the V *L* (or 2p X-ray absorption) edge and O *K* edge near-edge X-ray absorption fine structure (NEXAFS) spectra of the LVO samples. The V *L* edge is located at ~ 515 eV, which implies that the O K-edge data are found in the tail of the V $L_{2,3}$-edge, which complicates subsequent analysis. According to the refinement results, V is located at a 2c tetrahedral site within the Pmn21 structure and is in the + 5 oxidation state, thereby maintaining charge neutrality. A corresponding amount of V^{5+} is reduced to V^{4+} upon W^{6+} doping. V^{4+} has a $3d^1$ (t_{2g}^1 e_g^0) ground state with a partly filled spin-up t_{2g} shell, whereas V^{5+} has a $3d^0$ (t_{2g}^0 e_g^0) ground state; hence, unfilled t_g^2 and Eg features are observed. Overall, the V–L spectra, which do not show any discernible changes in position, exhibit a notable decrease in intensity upon W doping. SXR is a surface-characterization technique that only probes the particle surface, which contains more W and less V, as evidenced by the EDS data. Given that V^{5+} has four Eg states and six t_g^2 states, the effects of degeneracy and overlap in σ* and π* are significant at the O K-edge. Notably, despite the decrease in intensity, the σ* and π* intensity ratios remain almost unchanged; π* tends to exist at a slightly higher energy in the doped LVO samples, which suggests that stronger W − O bonds contribute.

The valence states of pristine and doped LVO were investigated by X-ray photoelectron spectroscopy (XPS). The deconvoluted V 2p spectra of pristine LVO and 10-LVO are shown in Fig. 4a and 4b, respectively. The fitted V 2p XPS spectrum of the pristine sample reveals two distinct peaks at 517.0 and 524.5 eV that correspond to the V $2p_{3/2}$ and V $2p_{1/2}$ states of V^{5+}. Two doublets that correspond to the V $2p_{1/2}$ and V $2p_{3/2}$ states of V^{4+} and V^{5+} are observed in the spectrum of the W-doped sample, which suggests that V^{5+} is partially reduced to V^{4+} [23], and is ascribable to a charge-compensation process owing to the higher valence of the W^{6+} dopant. The relationship between W^{6+}-dopant concentration and V^{4+} percentage is shown in Fig. 4c, which reveals that the V^{4+} percentage gradually rises with increasing dopant concentration. The proportion of V^{4+} eventually becomes saturated at a level of approximately 11.7 %. Fig. 4d shows W 4f spectra for all samples; deconvolution reveals that all doped samples contain W ions in the W^{6+} state, with W $4f_{7/2}$ and W $4f_{5/2}$ binding energy of 34.1 and 36.2 eV, respectively, and peak intensities proportionally related to dopant concentration. Conversely, these signals are absent in the spectrum of pristine sample, providing clear evidence that W^{6+} ions had been successfully doped into LVO. It is worth mentioning that the peak centered

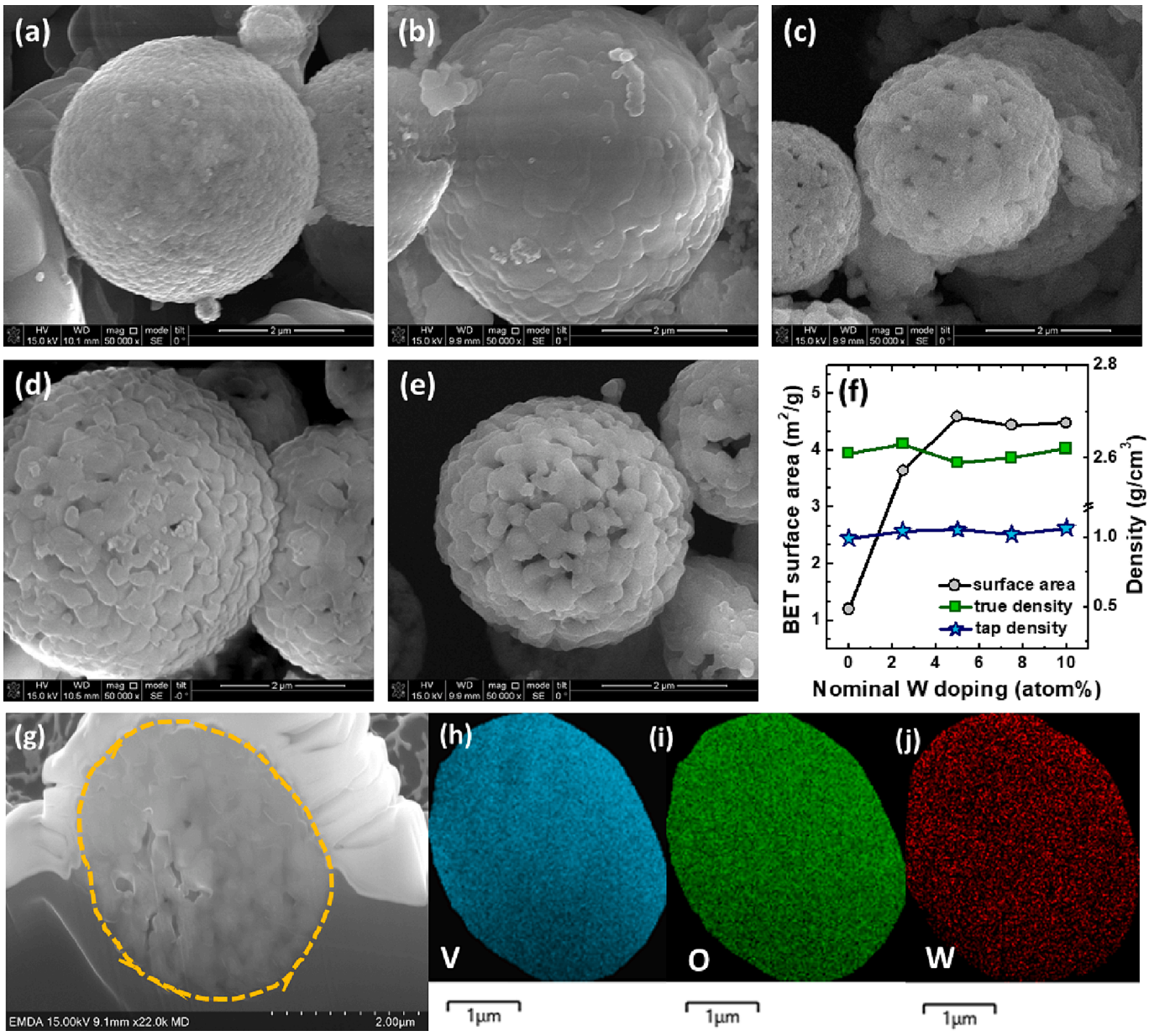

Fig. 2. W^{6+}-doped LVO morphologies. SEM images of (a) LVO, (b) 20.5-LVO, (c) 5-LVO, (d) 70.5-LVO, and (e) 10-LVO. (f) Surface areas, true densities, and tapping densities of the modified LVO samples. (g) FIB-SEM image of 5-LVO with associated (h) V, (i) O and (j) W EDS elemental maps. Scale bars: 1 μm.

at 41.2 eV in the XPS spectrum of each sample is attributable to the V 3p state [24]. The UV–vis diffuse reflectance spectra of these samples were also recorded to evaluate their bandgaps (E_g) according to the Tauc relationship [25]. As depicted in Fig. 4e, the doped samples exhibit more pronounced absorption in the 315–500 nm range compared to the pristine sample. The E_g values of LVO, 20.5-LVO, 5-LVO, 70.5-LVO, and 10-LVO were determined to be 30.90, 30.85, 30.77, 30.72, and 3.71 eV, respectively (Fig. 4f). These findings imply that doping with W^{6+} effectively modifies the electronic structure of LVO, resulting in bandgap shrinkage. This reduction in the bandgap has the potential to enhance conductivity and facilitate improved charge transfer [26].

Cyclic voltammetry (CV) was used to explore the electrochemical characteristics of the five samples. Fig. 5a shows that 5-LVO exhibits the largest CV loop, suggestive of the highest electrochemical activity among the samples. The CV profile of 5-LVO shows two anodic oxidation peaks at approximately 1.07 and 1.35 eV, while two corresponding reduction peaks are also observed at 0.9 and 0.55 eV during the cathodic sweep. The transition between V^{3+} and V^{5+} during lithiation/delithiation is responsible for the two redox couples [27], as described by Eq. (1):

$$Li_3VO_4 + xLi^+ + xe^- \leftrightarrow Li_{3+x}VO_4 (0 \leqslant x \leqslant 2) \quad (1)$$

In addition, voltage-difference polarizations of 0.53, 0.49, 0.45, 0.46, and 0.49 V between the second redox couple (O_2 and R_2) were determined for these samples as the W^{6+}-doping concentration was increased from 0 to 10 at%, respectively, which indicates that LVO conductivity can be enhanced by incorporating W^{6+} ions, leading to lower polarization. However, excessive W^{6+} doping led to a higher polarization; hence, the optimal W^{6+} concentration was determined to be 5 at%. Fig. 5b shows peak current–density (O_2) scan plots for the pristine and doped samples. 5-LVO exhibits the largest slope and, consequently, the best electrochemical kinetics, which declined as the W^{6+} concentration surpassed 5 at%. The CV profiles of pristine LVO and 5-LVO at various scan rates are shown in Fig. 5c and d, respectively. The adverse effects associated with excessively high doping concentrations likely stem from the formation of impure phases (VC) and lattice distortions.

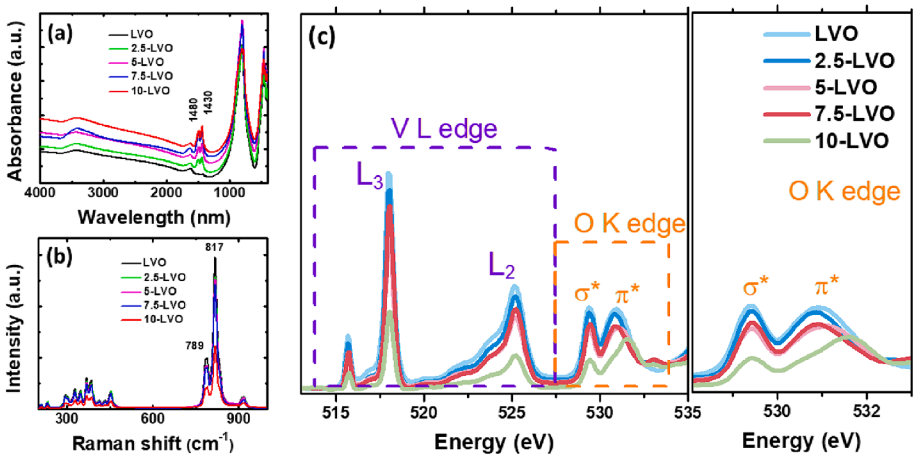

Fig. 3. Modified LVO spectroscopy. (a) FTIR, (b) Raman, and (c) V L and O K edge spectra of LVO electrodes at various W-doping concentrations.

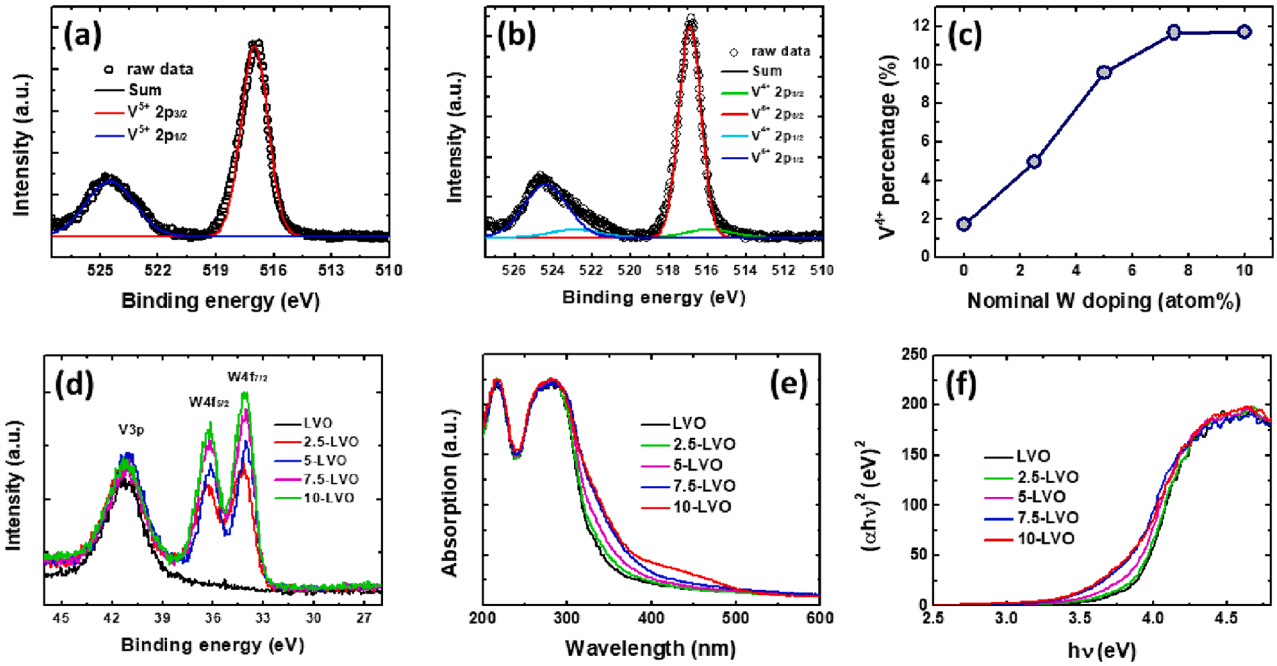

Fig. 4. Chemical states and bandgaps of as-prepared LVO samples. Deconvoluted V 2p XPS spectra of (a) LVO and (b) 5-LVO. (c) V^{4+} content as a function of W^{6+}-doping concentration. (d) W 4f XPS spectra of modified LVO samples. (e) UV–vis diffuse reflectance spectra and (f) corresponding Tauc plots of the various LVO samples.

The current recorded by CV can be interpreted as a combination of the current associated with a slow diffusion-controlled process and a rapid capacitive process [28]. According to the current-separation method developed by Wang and coworkers [29], the current response at a fixed voltage can be expressed using Eq. (2):

$$i(V) = k_1 u + k_2 u^{1/2} \tag{2}$$

where $k_1\upsilon$ and $k_2\upsilon^{1/2}$ represent the current contributions of the capacitive- and diffusion-controlled processes, respectively. The capacitive contribution of 5-LVO at a scan rate of 0.1 mV/s accounts for 63.9 % of the total capacity and arises from the diffusion-controlled contribution (Fig. 5e), which suggests that the diffusion-controlled process plays a significant role in the lithiation/delithiation reactions. The contribution ratios of the two distinct electrochemical processes were evaluated at various scan rates. The energy-storage mechanism of 5-LVO was found to be highly dependent on scan rate (Fig. 5f), with the capacitive capacity steadily increasing with increasing scan rate.

Electrochemical impedance spectroscopy (EIS) was used to further explore the impact of W^{6+} doping on the electrochemical characteristics of LVO. Fig. 6a displays typical Nyquist plots of the five samples. All Nyquist plot show dispersed semicircles and inclined lines with similar electrolyte resistances, which are interpreted as the charge-transfer resistance (R_{ct}) and Warburg impedance [30,31]. The doped samples have significantly lower R_{ct} values than the pristine sample; 5-LVO exhibits the smallest value (57.5 Ω), suggestive of a rapid charge-transfer process. The Li^+-diffusion coefficients (D_{Li}) of the doped LVO samples were also assessed from the Warburg regions of the EIS plots using Eqs. (3) and (4), respectively:

$$Z_{re} = R_{ct} + R_s + sw^{-1/2} \tag{3}$$

$$D_{Li} = R^2T^2/2A^2n^4F^4C^2s^2 \tag{4}$$

According to Eq. (3), the σ value is obtained from the slope of the relationship between Z_{re} and $\omega^{-1/2}$, as shown in Fig. 6b. 5-LVO exhibited

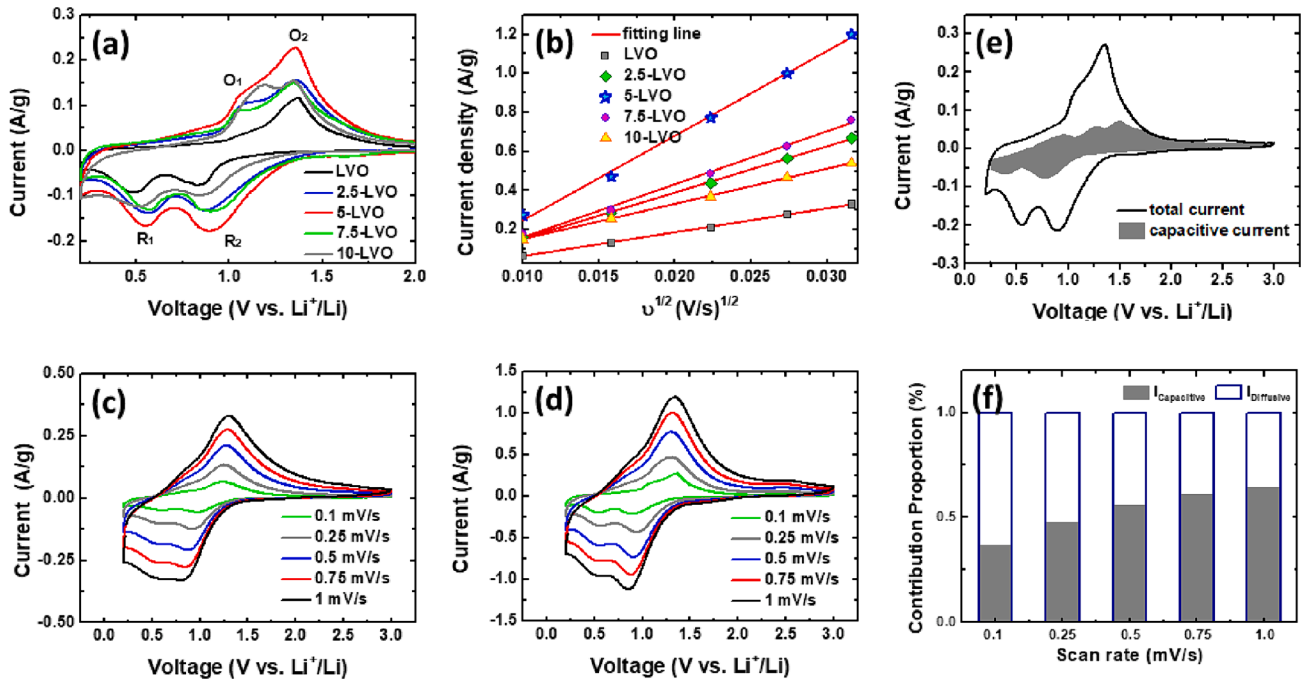

Fig. 5. Electrochemically characterizing as-prepared LVO samples. (a) CV traces of the five samples. (b) Linear relationships between anodic peak current density and the square root of scan rate ($\upsilon^{1/2}$). CV traces of (c) LVO and (d) 5-LVO at various scan rates. (e) Contribution of capacitive-controlled capacities (gray shaded region) in the CV trace of 5-LVO acquired at 0.1 mV/s. (f) Contributions of capacitive and diffusion-controlled capacities of 5-LVO at various scan rates.

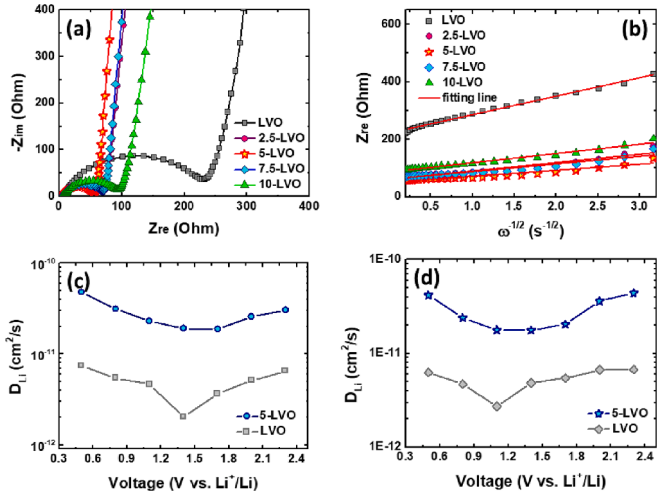

Fig. 6. Electrochemical kinetics of as-prepared LVO samples. (a) Nyquist plots of pristine and doped LVO samples. (b) Plots of the real part of complex impedance versus $\omega^{-1/2}$. Li^+-diffusion coefficients (D_{Li}) of pristine LVO and 5-LVO as functions of voltage during (c) charging and (d) discharging.

the largest D_{Li} value of 4.54×10^{-11} cm^2/s, which is 8.66 times larger than that of pristine LVO (5.24×10^{-12} cm^2/s). In addition, the D_{Li} values of LVO and 5-LVO were determined at different voltages using the potentiostatic intermittent titration technique (PITT) [32], and the voltage dependences of the D_{Li} values for pristine LVO and 5-LVO were determined using Eq. (5) from the slope of the ln I(t) vs. t relationship in the linear region.

$$D_{Li} = \frac{d\ln(I)}{dt} \cdot \left(\frac{2}{\pi}\right)^2 \cdot \left(\frac{V_M n_B}{S}\right)^2 \quad (5)$$

where I(t) denotes the transient current (Fig. S2), V_M is the molar volume of the active material (53.4 cm^3/mol), n_B is the number of moles (1.21×10^{-5} mol), and S is the electrode surface area (1.33 cm^2). Fig. 6c and d show how the D_{Li} values of LVO and 5-LVO vary during charging and discharging, which reveal that the D_{Li} value of 5-LVO is always higher than that of pristine LVO during lithiation/delithiation. 5-LVO exhibits D_{Li} values that range between 1.86×10^{-11} and 4.78×10^{-11} cm^2/s, and 1.76×10^{-11} and 4.4×10^{-11} cm^2/s, during charging and discharging, respectively, which are close to the values obtained by EIS and indicate that 5-LVO exhibits faster Li^+ migration than pristine LVO.

Electronic density of states (DOS) were calculated using density functional theory (DFT) and used to explore the effect of W^{6+} doping on the electronic conductivity of LVO. Fig. 7 compares the electronic densities of states of $Li_{48}V_{16}O_{64}$ and $Li_{48}V_{15}W_1O_{64}$. The former exhibits a wide gap (~4.0 eV) between the valence and conduction bands, and the projected partial DOS on each atom further shows that the conduction-band minimum of LVO is mainly composed of the d- and p-orbitals of V and O, respectively, whereas the p-orbital of O contributes to the valence-band maximum. A sharp peak is observed at approximately 3.0 eV above the valance band maximum when a single V in the matrix is replaced by W. The existence of this mid-gap state provides a reasonable explanation for the higher conductivity observed for W-doped LVO [33]. Surprisingly, the DOS projection shows that the W atom in the matrix contributes to this mid-gap state rather than the V and O atoms. The doping behavior was further examined based on the partial charge density and inferior charge states of $Li_{48}V_{15}W_1O_{64}$, the results of which are summarized in Fig. S3.

The galvanostatic charge–discharge (GCD) profiles of the pristine LVO and 5-LVO electrodes at various C rates are presented in Fig. 8a and b, respectively. Both the pristine and modified LVOs exhibit operating voltages of approximately 1.05 V, which assures safety by thermodynamically inhibiting the growth of dendritic lithium. Both electrodes are seen to deliver a specific capacity of approximately 403 mAh/g at a current density of 0.1C. Nevertheless, the 5-LVO electrode displays a significantly larger capacity of 288.9 mAh/g at a high current density of 10C that surpasses that of the pristine LVO electrode by a factor of 10.52. Furthermore, the GCD profiles show that 5-LVO is less electrochemically polarized than the pristine sample. Fig. 8c shows polarization values for the two electrodes as functions of C-rate. The pristine sample is more

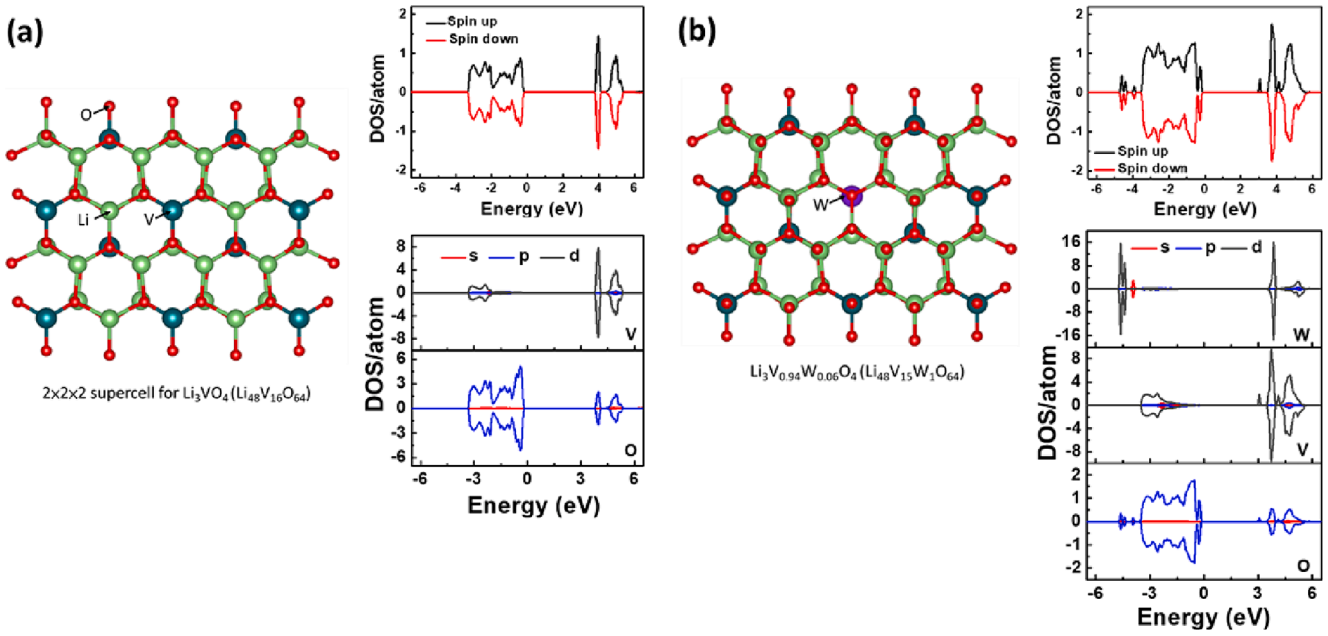

Fig. 7. DFT calculations of a modified LVO. Electronic densities of states for (a) pristine $Li_{48}V_{16}O_{64}$ and (b) W-doped $Li_{48}V_{15}W_1O_{64}$.

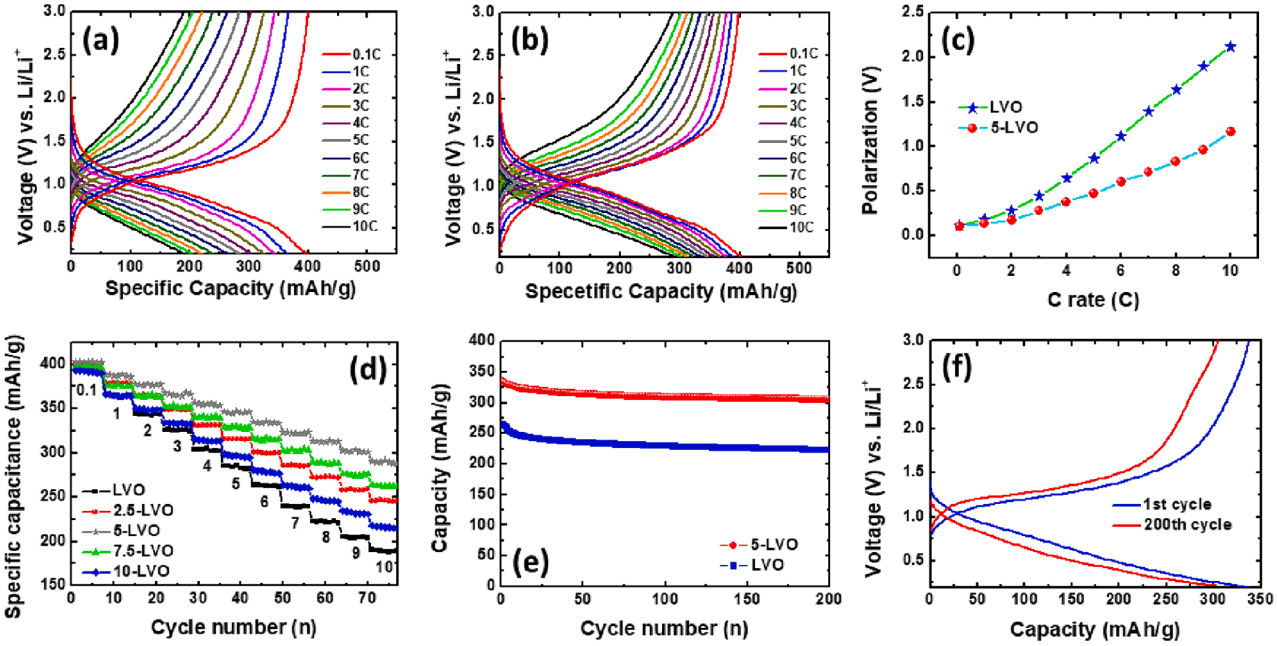

Fig. 8. Energy-storage performance of modified LVOs. GCD profiles for (a) pristine LVO and (b) 5-LVO at various C rates. (c) Polarization versus C-rate curves for LVO and 5-LVO. (d) Rate performance of the five samples in this study. (e) Cycling performance of LVO and 5-LVO at 6C and (f) corresponding GCD profiles of 5-LVO acquired during the first and last cycles.

polarized than 5-LVO, with the difference in polarization increasing with increasing current density. The rate performance of all five electrodes at different C-rates in the 0.1–10C range is displayed in Fig. 8d. All doped samples exhibit better rate capabilities than the pristine LVO electrode. Remarkably, the 5-LVO electrode displays the best rate performance among the investigated samples, which is consistent with the aforementioned results. LVO, 20.5-LVO, 5-LVO, 70.5-LVO, and 10-LVO exhibited discharge capacities of 1890.0, 2460.6, 2880.9, 2620.4, and 216.3 mAh/g, respectively, at a high current density of 10C. The relatively low degree of polarization and faster electrochemical kinetics of 5-LVO originate from a dramatically higher electrical conductivity owing to the presence of a mixed V valence state (V^{4+} and V^{5+}). The electrochemical properties of 5-LVO compared with other modified LVOs from the literature are listed in Table S6. Furthermore, the cycling stabilities of LVO and 5-LVO at 6C are shown in Fig. 8e. The discharge capacities of the LVO and 5-LVO electrodes decreased from 264.2 to 222.8 mAh/g and 334.5 to 305.8 mAh/g, respectively, over 200 cycles, which correspond to capacity losses of 15.6 % and 8.6 %, respectively, and highlights the superior cycling stability of the 5-LVO electrode. The corresponding GCD profiles of 5-LVO during the initial and final cycles are shown in Fig. 8f.

We finally fabricated a full LIB and a hybrid LIC based on 5-LVO to demonstrate its practicality. The full LIB was assembled using 5-LVO as the anode and LNMO as the cathode, with CV used to evaluate the

working potential window of each electrode in a half-cell configuration, the results of which are shown in Fig. 9a. LNMO exhibits two redox couples at 40.73/4.63 V and 40.80/4.68 V that are ascribable to Ni^{2+}/Ni^{3+} and Ni^{3+}/Ni^{4+} transitions, respectively [34], resulting in an average working potential of 4.71 V (Li^+/Li). The 5-LVO//LNMO LIB delivered an operating voltage of 3.66 V by combining LNMO and 5-LVO at a working potential of 1.05 V (Li^+/Li). The GCD profiles of LNMO and 5-LVO acquired at 0.1C are displayed in Fig. 9b. LNMO has a discharge capacity of 133.4 mAh/g; hence, the profiles further show that the 5-LVO-anode/LNMO-cathode combination delivers a 3.66 V LIB. Fig. 9c displays CV traces for the 5-LVO//LNMO LIB at various scan rates between 2.2 and 4.5 V. Broad redox peaks are observed at 3.4 – 3.9 V that are ascribable to the following dominant reversible reaction [35]:

$$Li_3VO_4 + LiNi_{0.5}Mn_{1.5}O_4 \leftrightarrow Li_{3+x}VO_4 + Li_{1-x}Ni_{0.5}Mn_{1.5}O_4 \quad (6)$$

The linear relationship between the peak current and the square root of the scan rate (Fig. S4) indicates that the corresponding redox reaction is diffusion-controlled. The GCD traces and rate performance of the full LIB are shown in Fig. 9d and e, respectively. A specific capacity of 355.8 mAh/g was recorded at 0.2C based on the mass of the 5-LVO anode, with 57.8 % of the capacity (205.8 mAh/g) still retained at 8C (Fig. 9e), highlighting its remarkable rate capability. The excellent cycling stability of the 5-LVO//LNMO LIB is also demonstrated in Fig. 9f. The LIB still delivered a capacity of 219.1 mAh/g after 200 cycles at 5C, which is about 79.6 % of the initial value.

In addition, a hybrid LIC was assembled using 5-LVO and AC as the anode and cathode electrodes, and 1.0 M $LiPF_6$ EC/DMC (1:1) as the electrolyte (Fig. 10a). The CV trace and the corresponding GCD profile of the AC electrode are shown in Fig. 10b and c, respectively, and were used to balance the charge between the anode and cathode. The rectangular CV curve and symmetrical GCD profile recorded for the AC electrode are consistent with its electric double-layer capacitor (EDLC) nature. The specific capacity of the AC was calculated to be 62.9 mAh/g based on the GCD profile (Fig. 10c). Charge balance in the hybrid LIC should follow the equation [36]:

$$m^+C^+ = m^-C^- \quad (7)$$

where m and Q are the mass of the active material in each electrode and the specific capacity, respectively. The specific capacities of the 5-LVO and AC used in this study are 403 and 62.9 mAh/g, respectively. Consequently, the optimal mass ratio between the 5-LVO and AC electrodes was maintained at 1:60.4. Fig. 10d shows CV traces for the 5-LVO//AC LIC at 10 mV/s operated at various operational voltages in the 10.7–4.5 V range to determine the best operating voltage of the LIC. A sharp rise in current density is observed at 40.2–4.5 V when the voltage window is extended to 4.5 V, which suggests that the system is unstable under such conditions. Therefore, the optimal voltage window for the LIC was determined to be 10.7–4.5 V. CV traces for the 5-LVO//AC LIC acquired at various scan rates are displayed in Fig. 10e. All CV traces exhibit similar shapes and are not severely distorted, which demonstrates the excellent electrochemical properties and high rate capability of the 5-LVO//AC LIC. Typical GCD profiles of the LIC in various voltage windows are shown in Fig. 10f. The CV results reveal that the discharge time significantly increases as the operating voltage window is expanded from 1.7 – 3.0 to 1.7 – 4.2 V. Extending the operating voltage window in such a manner dramatically boosts the energy density from 33.6 to 135.8 Wh/kg, which corresponds to an increase of over 400 % (Fig. 10g). Fig. 10*h* shows charge–discharge profiles of the LIC at various current densities in the 0.1–4 A/g range and a voltage window of 10.7–4.2 V. The LIC exhibited specific capacitances of 550.4, 420.2, 380.4, 350.1, 32, and 30.4F/g at current densities of 0.1, 0.5, 1, 2, 3, and 4 A/g, respectively, based on the total mass of the positive and negative electrodes. A hybrid LIC composed of LIB-type and EDLC-type electrodes is well known to combine the advantages of both LIBs and SCs. Hence, the hybrid LIC displays unique performance in the middle of the spectrum in terms of power and energy density. The Ragone plot of the 5-LVO//AC LIC derived from its discharge curves is displayed in Fig. 10i. A maximum energy density of 131.8 Wh/kg was obtained at a power density of 295 W/kg; this energy density rivals reported values, including those of LVO-based LICs: AC//Li_3VO_4@C (129.7 Wh/kg) [37], *hp*-LVO/C//CMK-3 (105 Wh/kg) [38], LVO//AC (122.2 Wh/kg) [39], Li_3VO_4/CNFs//graphene (110 Wh/kg) [40], AC//LVO/C (110 Wh/kg) [41], Li_3VO_4//AC (136.4 Wh/kg) [42]; TNO based LICs: $TiNb_2O_{7-x}$//SCCB (114 Wh/kg) [43]; $TiNb_2O_7$/rGO//AC (127 Wh/kg) [44]; TNO/HG//AC (86.3 Wh/kg) [45], AC/$TiNb_2O_7$ (43 Wh/kg) [46], TNO@C//CFs (110.4 Wh/kg) [47], and LTO based LICs: LTO-G-

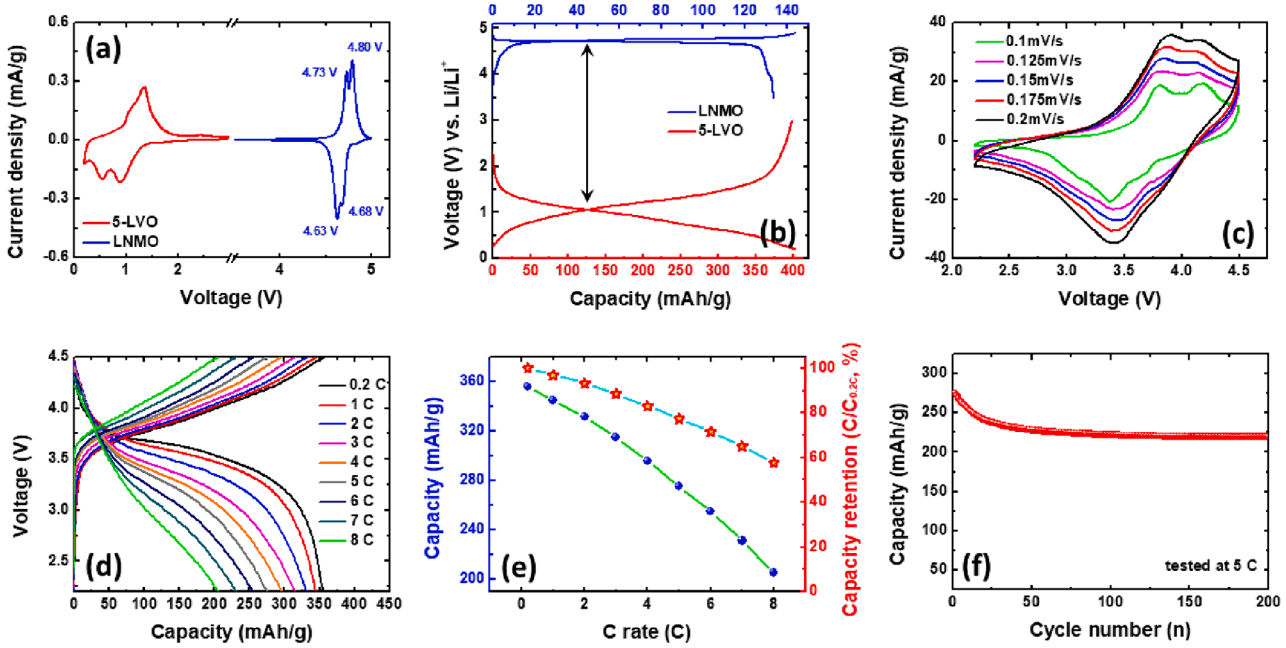

Fig. 9. 5-LVO//LNMO full-LIB performance. (a) Typical CV traces for the 5-LVO- and LNMO-based half cells. (b) Comparing GCD profiles of 5-LVO and LNMO. (c) CV profiles of a Cr-TNO//LNMO full cell acquired at various scan rates. (d) GCD profiles of the full cell are acquired at various C rates. (e) Rate and (f) cycling performance of the 5-LVO//LNMO full cell at 5C.

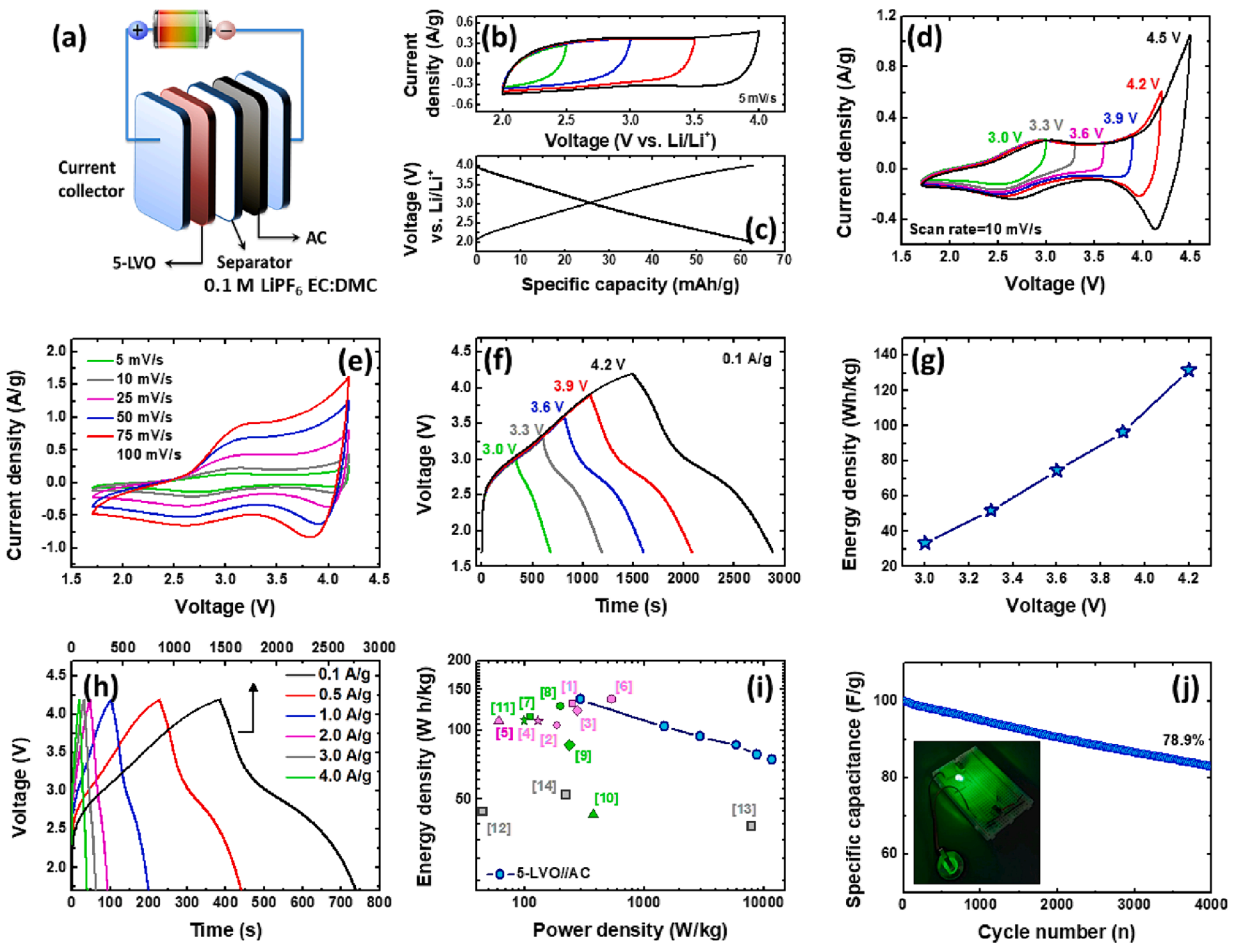

Fig. 10. 5-LVO//AC LIC performance. (a) Schematic representation of the 5-LVO//AC LIC. (b) CV traces of the AC acquired in various voltage windows. (c) GCD profile of the AC at 0.1 A/g. (d) CV traces were acquired for the 5-LVO//AC LIC in various voltage windows. (e) CV traces of the LIC were acquired at various scan rates. (f) GCD profiles of the LIC acquired in various voltage windows. (g) LIC energy density as a function of voltage window at a fixed current density of 0.1 A/g. (h) GCD profiles were acquired at various current densities. (i) Ragone plot of the 5-LVO//AC LIC and (j) cycling performance over 5000 cycles at 2.0 A/g (inset: digital photograph of an LED powered by the LIC).

600//AC (44 Wh/kg) [48], AC//LTO-AC-3 (38 Wh/kg) [49], and 100-LTO-G-600C//AC (52 Wh/kg) [50]. The cycling performance of the LIC is shown in Fig. 10j, which demonstrates a superior capacitance retention of 78.9 % after 5000 cycles at a current density of 2 A/g. A single LIC drove a light-emitting diode, as shown in the inset of Fig. 10j, which highlights its potential use in practical applications.

4. Conclusion

W^{6+}-doped LVO anode materials were prepared using a spray-drying method. Introduction of the W^{6+} dopant into the LVO lattice roughened the LVO surface morphology and led to a narrower bandgap, resulting in enhanced conductivity and the facilitation of Li^{+}-ion migration. The 5-LVO microspheres exhibited a high discharge capacity of 288.9 mAh/g at 10C and good cycling stability, with a retention of 91.4 % observed after 200 cycles at 6C. When paired with an LNMO cathode, a full 5-LVO//LNMO LIB delivered a specific capacity of 355.8 mAh/g at 0.2C and 205.8 mAh/g at 8C, with a voltage of 3.7 V. Furthermore, 5-LVO//AC LICs were assembled to evaluate their practical potential. The 5-LVO-anode/AV-cathode combination displayed an impressive operation voltage of 4.2 V and delivered an energy density of 135.8 Wh/kg at a power density of 295 W/kg. These results demonstrate the significant potential of the spray-dried 5-LVO as a high-performance material for use in energy-storage applications.

CRediT authorship contribution statement

Yu-Sheng Hsiao: Writing – review & editing, Writing – original draft, Supervision, Resources, Project administration, Investigation, Formal analysis, Conceptualization. **Jen-Hsien Huang:** Writing – original draft, Visualization, Methodology, Formal analysis, Data curation, Conceptualization. **Lin-Yang Weng:** Investigation, Formal analysis, Data curation. **Ta-Hung Cheng:** Formal analysis, Data curation. **Han-Hsin Chiang:** Formal analysis, Data curation. **Cheng-Zhang Lu:** Formal analysis, Data curation. **Huei-Chu Weng:** Supervision. **Lars Thomsen:** Formal analysis, Data curation. **Bruce Cowie:** Formal analysis, Data curation. **Wei Kong Pang:** Writing – review & editing, Supervision, Resources, Formal analysis, Data curation. **Yu-Ching Huang:** Supervision, Resources.

Declaration of competing interest

The authors declare that they have no known competing financial interests or personal relationships that could have appeared to influence the work reported in this paper.

Data availability

The data that has been used is confidential.

Acknowledgments

These research endeavors were supported by the National Science and Technology Council (NSTC) of Taiwan (grant nos.: MOST 111-2628-E-011-003-MY2). We thank the National Center for High-Performance Computing in Taiwan for its high-performance computing facilities. W.K.P. acknowledges support from the Australian Research Council (ARC) for DP230100198 and LE210100109. Part of the work was carried out at the Soft X-ray (SXR) beamline (beamtime: M19450 and M18254) at the Australian Synchrotron, and Echidna (beamtime: MI12623) at the Australian Centre for Neutron Scattering under merit programs. The authors acknowledge the operational support of ANSTO staff, especially Prof. Vanessa K. Peterson, for collecting high-resolution NPD data.

Appendix A. Supplementary data

Supplementary data to this article can be found online at https://doi.org/10.1016/j.cej.2024.150973.

References

[1] L. Wu, X. Leng, Y. Liu, S. Wei, C. Li, G. Wang, J. Lian, Q. Jiang, A. Nie, T.Y. Zhang, A strategy for synthesis of nanosheets consisting of alternating spinel $Li_4Ti_5O_{12}$ and rutile TiO_2 lamellas for high-rate anodes of lithium-ion batteries, ACS Applied Materials & Interfaces 9 (2017) 4649–4657.

[2] Z.N. Ezhyeh, M. Khodaei, F. Torabi, Review on doping strategy in $Li_4Ti_5O_{12}$ as an anode material for Lithium-ion batteries, Ceramics International 49 (2023) 7105–7141.

[3] L. Bai, B. Pan, F. Song, Q. Chen, Co/S co-doped $Li_4Ti_5O_{12}$ as lithium-ion batteries anode for high-rate, J. Energy Storage 73 (2023) 109155.

[4] G. Yu, Q. Zhang, J. Jing, X. Wang, Y. Li, X. Bai, T. Li, Bulk modification of porous $TiNb_2O_7$ microsphere to achieve superior lithium-storage properties at low temperature, Small 22 (2023) 2303087.

[5] Y. Wu, D. Liu, D. Qu, J. Li, Z. Xie, X. Zhang, H. Chen, H. Tang, Porous oxygen-deficient $TiNb_2O_7$ spheres wrapped by MXene as high-rate and durable anodes for liquid and all-solid-state lithium-ion batteries, Chemical Engineering Journal 438 (2022) 135328.

[6] X. Bai, D. Zhang, Z. Xiong, S. Yang, C. Pei, B. Sun, S. Ni, Construction of hierarchical Li_3VO_4/NC sponge structure for high-performance lithium storage, Electrochimica Acta 462 (2023) 142807.

[7] S. Ni, J. Zhang, J. Ma, X. Yang, L. Zhang, X. Li, H. Zeng, Approaching the theoretical capacity of Li_3VO_4 via electrochemical reconstruction, Advanced Materials Interfaces 3 (2016) 1500340.

[8] E. Dompablo, P. Tartaj, M. Amarilla, U. Amador, Computational investigation of li insertion in Li_3VO_4, Chemistry of Materials 28 (2016) 5643–5651.

[9] M. Yan, D. Zhang, Q. Ouyang, X. Zhang, Y. Wang, X. Zhao, G. Li a, L. Li, Fabricating oxygen vacancy-rich Li_3VO_4 nanoplates to improve electrochemical performance, Electrochimica Acta 470 (2023) 143303.

[10] Y. Shi, J.Z. Wang, S.L. Chou, D. Wexler, H.J. Li, K. Ozawa, H.K. Liu, Y.P. Wu, Hollow structured Li_3VO_4 wrapped with graphene nanosheets in situ prepared by a one-pot template-free method as an anode for lithium-ion batteries, Nano Letters 13 (2013) 4715–4720.

[11] Q. Li, Q. Wei, J. Sheng, M. Yan, L. Zhou, W. Luo, R. Sun, L. Mai, Mesoporous Li_3VO_4/C submicron-ellipsoids supported on reduced graphene oxide as practical anode for high-power lithium-ion batteries, Advancement of Science 2 (2015) 1500284.

[12] X. Wang, B. Qin, D. Sui, Z. Sun, Y. Zhou, H. Zhang, Y. Chen, Facile synthesis of carbon-coated Li_3VO_4 anode material and its application in full cells, Energy Technol. 6 (2018) 2074–2081.

[13] Z. Jian, M. Zheng, Y. Liang, X. Zhang, S. Gheytani, Y. Lan, Y. Shi, Y. Yao, Li_3VO_4 anchored graphene nanosheets for long-life and high-rate lithium-ion batteries, Chemical Communications 51 (2015) 229–231.

[14] Y. Yang, J. Li, D. Chen, J. Zhao, Spray drying-assisted synthesis of Li_3VO_4/C/CNTs composites for high-performance lithium ion battery anodes, Journal of the Electrochemical Society 164 (2017) A6001–A6006.

[15] L. Zhao, H. Duan, Y. Zhao, Q. Kuanga, Q. Fan, L. Chen, Y. Dong, High capacity and stability of nb-doped Li_3VO_4 as an anode material for lithium ion batteries, Journal of Power Sources 378 (2018) 618–627.

[16] Y. Dong, H. Duan, K. Park, Y. Zhao, Mo6+ doping in Li3VO4 anode for li-ion batteries: significantly improve the reversible capacity and rate performance, ACS Applied Materials & Interfaces 9 (2017) 27688–27696.

[17] B. Dong, R. Jarkaneh, S. Hull, N. Reeves-McLaren, J.J. Biendicho, A.R. West, Synthesis, structure and electrical properties of N-doped Li_3VO_4, Journal of Materials Chemistry A 4 (2016) 1408–1413.

[18] D. Schweke, Y. Mordehovitz, M. Halabi, L. Shelly, S. Hayun, Defect chemistry of oxides for energy applications, Advanced Materials 30 (2018) 1706300.

[19] Y. Liu, T. Zeng, G. Li, T. Wan, M. Li, X. Zhang, M. Li, M. Su, A. Dou, W. Zeng, Y. Zhou, R. Guo, D. Chu, The surface double-coupling on single-crystal $LiNi_{0.8}Co_{0.1}Mn_{0.1}O_2$ for inhibiting the formation of intragranular cracks and oxygen vacancies, Energy Storage Materials 52 (2022) 534–546.

[20] G. Yang, B. Zhang, J. Feng, Y. Lu, Z. Wang, V. Aravindan, M. Aravind, J. Liu, M. Srinivasan, Z. Shen, Y. Huang, Morphology controlled lithium storage in Li_3VO_4 anode, Journal of Materials Chemistry A 6 (2018) 456–463.

[21] Q. Fu, F. Du, X. Bian, Y. Wang, X. Yan, Y. Zhang, K. Zhu, G. Chen, C. Wang, Y. Wei, Electrochemical performance and thermal stability of $Li_{1.18}Co_{0.15}Ni_{0.15}Mn_{0.52}O_2$ surface coated with the ionic conductor Li_3VO_4, Journal of Materials Chemistry A 2 (2014) 7555–7562.

[22] C.C. Yang, H.C. Hu, S.J. Lin, W.C. Chien, Electrochemical performance of V-doped spinel $Li_4Ti_5O_{12}$/C composite anode in li-half and $Li_4Ti_5O_{12}$/$LiFePO_4$-full cell, Journal of Power Sources 258 (2014) 424–433.

[23] H. Yu, J. Zeng, W. Hao, P. Zhou, X. Wen, Mo-doped V_2O_5 hierarchical nanorod/nanoparticle core/shell porous microspheres with improved performance for cathode of lithium-ion battery, Journal of Nanoparticle Research 20 (2018) 135.

[24] F.Y. Kong, M. Li, S.S. Pan, Y.X. Zhang, G.H. Li, Synthesis and thermal stability of W-doped VO_2 nanocrystals, Materials Research Bulletin 46 (2011) 2100–2104.

[25] X. Liu, G. Li, D. Zhang, D. Chen, X. Wang, B. Li, L. Li, Fe-doped Li_3VO_4 as an excellent anode material for lithium ion batteries: optimizing rate capability and cycling stability, Electrochimica Acta 308 (2019) 185–194.

[26] X. Liu, G. Li, D. Zhang, L. Meng, B. Li, L. Li, F doped Li_3VO_4: an advanced anode material with optimized rate capability and durable lifetime, Electrochimica Acta 354 (2020) 136655.

[27] E. Thauer, G.S. Zakharova, S.A. Wegener, Q. Zhu, R. Klingeler, Sol-gel synthesis of Li_3VO_4/C composites as anode materials for lithium-ion batteries, Journal of Alloys and Compounds 853 (2021) 157364.

[28] X. Xu, F. Niu, C. Wang, Y. Li, C. Zhao, J. Yang, Y. Qian, Li_3VO_4 nanoparticles in N-doped carbon with porous structure as an advanced anode material for lithium-ion batteries, Chemical Engineering Journal 370 (2019) 606–613.

[29] J. Wang, J. Polleux, J. Lim, B. Dunn, Pseudocapacitive contributions to electrochemical energy storage in TiO2 (anatase) nanoparticles, Journal of Physical Chemistry C 111 (2007) 14925–14931.

[30] G. Zha, N. Hu, Y. Luo, F. Wang, R. Wu, Y. Li, H. Fu, X. Fu, Reducing Ni/Li disorder and boosting electrochemical performance of $LiNi_{0.8}Co_{0.067}Fe_{0.033}Mn_{0.1}O_2$ cathode material, Journal of the Taiwan Institute of Chemical Engineers 144 (2023) 104730.

[31] X. Qu, H. Huang, T. Wan, L. Hu, Z. Yu, Y. Liu, A. Dou, Y. Zhou, M. Su, X. Peng, H. H. Wu, T. Wu, D. Chu, An integrated surface coating strategy to enhance the electrochemical performance of nickel-rich layered cathodes, Nano Energy 91 (2022) 106665.

[32] L.L. Zhou, S.Y. Shen, X. Peng, L.N. Wu, Q. Wang, C.H. Shen, T.T. Tu, L. Huang, J. T. Li, S.G. Sun, New insights into the structure changes and interface properties of Li_3VO_4 anode for lithium ion batteries during the initial cycle by in-situ techniques, ACS Applied Materials & Interfaces 8 (2016) 23739–23745.

[33] Y. Zhou, H. Zhang, Y. Wang, T. Wan, P. Guan, X. Zhou, X. Wang, Y. Chen, H. Shi, A. Dou, M. Su, R. Guo, Y. Liu, L. Dai, D. Chu, Relieving stress concentration through anion−cation codoping toward highly stable nickel-rich cathode, ACS Nano 17 (2023) 20621–20633.

[34] G.B. Zhong, Y.Y. Wang, Y.Q. Yu, C.H. Chen, Electrochemical investigations of the LiNi0.45M0.10Mn1.45O4 (M = fe co, cr) 5 V cathode materials for lithium ion batteries, Journal of Power Sources 205 (2012) 385–393.

[35] L. Shen, S. Chen, J. Maier, Y. Yu, Carbon-coated Li_3VO_4 spheres as constituents of an advanced anode material for high-rate long-life lithium-ion batteries, Advanced Materials 29 (2017) 1701571.

[36] X. Wang, B. Liu, R. Liu, Q. Wang, X. Hou, D. Chen, R. Wang, G. Shen, Fiber-based flexible all-solid-state asymmetric supercapacitors for integrated photodetecting system, Angewandte Chemie, International Edition 53 (2014) 1849–1853.

[37] X. Ren, D. Ai, C. Zhan, R. Lv, F. Kang, Z.H. Huang, 3D porous Li_3VO_4@C composite anodes with ultra-high rate capacity for lithium-ion capacitors, Electrochimica Acta 355 (2020) 136819.

[38] X. Xu, F. Niu, D. Zhang, C. Chu, C. Wang, J. Yang, Y. Qian, Hierarchically porous Li_3VO_4/C nanocomposite as an advanced anode material for high-performance lithium-ion capacitors, Journal of Power Sources 384 (2018) 240–248.

[39] M. Zhang, L. Dong, C. Zhang, F. Yin, H. Peng, G. Wang, Heterogeneous nucleation of Li_3VO_4 regulated in dense graphene aerogel for lithium ion capacitors, Journal of Power Sources 468 (2020) 228364.

[40] F. Wang, Z. Liu, X. Yuan, J. Mo, C. Li, L. Fu, Y. Zhu, X. Wu, Y. Wu, A quasi-solid-state li-ion capacitor with high energy density based on Li_3VO_4/carbon nanofibers and electrochemically-exfoliated graphene sheets, Journal of Materials Chemistry A 5 (2017) 14922–14929.

[41] W. Liu, X. Zhang, C. Li, K. Wang, X. Sun, Y. Ma, Carbon-coated Li_3VO_4 with optimized structure as high capacity anode material for lithium-ion capacitors, Chinese Chemical Letters 31 (2020) 2225–2229.

[42] L. Shen, H. Lv, S. Chen, P. Kopold, P.A. van Aken, X. Wu, J. Maier, Y. Yu, Peapod-like Li_3VO_4/N-doped carbon nanowires with pseudocapacitive properties as advanced materials for high-energy lithium-ion capacitors, Advanced Materials 29 (2017) 1700142.

[43] W. Zhu, B. Zou, C. Zhang, D.H.L. Ng, S.A. El-Khodary, X. Liu, G. Li, J. Qiu, Y. Zhao, S. Yang, J. Lian, H. Li, Oxygen-defective $TiNb_2O_{7-x}$ nanochains with enlarged lattice spacing for high-rate lithium ion capacitor, Adv. Mater. Inter. 7 (2020) 2000705.

[44] Y. Li, Y. Wang, R. Cai, C. Yu, J. Zhang, J. Wu, C.S. Tiwary, J. Cui, Y. Zhang, Y. Wu, Pseudocapacitive $TiNb_2O_7$/reduced graphene oxide nanocomposite for high–rate lithium ion hybrid capacitors, Journal of Colloid and Interface Science 610 (2022) 385–394.

[45] X. Jiao, Q. Hao, X. Xia, D. Yao, Y. Ouyang, W. Lei, Boosting long-cycle-life energy storage with holey graphene supported $TiNb_2O_7$ network nanostructure for lithium ion hybrid supercapacitors, Journal of Power Sources 403 (2018) 66–75.
[46] V. Aravindan, J. Sundaramurthy, A. Jain, P.S. Kumar, W.C. Ling, S. Ramakrishna, M.P. Srinivasan, S. Madhavi, Unveiling $TiNb_2O_7$ as an insertion anode for lithium ion capacitors with high energy and power density, ChemSusChem 7 (2014) 1858–1863.
[47] X. Wang, G. Shen, Intercalation pseudo-capacitive $TiNb_2O_7$@carbonelectrode for high-performance lithium ion hybrid electrochemical supercapacitors with ultrahigh energy density, Nano Energy 15 (2015) 104–115.
[48] X. Zhang, C. Lu, H. Peng, X. Wang, Y. Zhang, Z. Wang, Y. Zhong, G. Wang, Influence of sintering temperature and graphene additives on the electrochemical performance of porous $Li_4Ti_5O_{12}$ anode for lithium ion capacitor, Electrochimica Acta 246 (2017) 1237–1247.
[49] C. Jiang, J. Zhao, H. Wu, Z. Zou, R. Huang, $Li4Ti_5O_{12}$/activated-carbon hybrid anodes prepared by in situ copolymerization and post-CO_2 activation for high power li-ion capacitors, Journal of Power Sources 401 (2018) 135–141.
[50] G. Wang, C. Lu, X. Zhang, B. Wan, H. Liu, M. Xia, H. Gou, G. Xin, J. Lian, Y. Zhang, Toward ultrafast lithium ion capacitors: a novel atomic layer deposition seeded preparation of $Li_4Ti_5O_{12}$/graphene anode, Nano Energy 36 (2017) 46–57.